A. De Gaspari, A. Mannarino, P. Mantegazza
A Dual Loop Strategy for the Design of a Control Surface Actuation System with Nonlinear Limitations
Mechanical Systems and Signal Processing, Vol. 90, 2017, p. 334-349
doi:10.1016/j.ymssp.2016.12.037

A Dual Loop Strategy For The Design of a Control Surface Actuation System with Nonlinear Limitations

Alessandro De Gaspari[a,1,*], Andrea Mannarino[a,2], Paolo Mantegazza[a,3]

[a]*Department of Aerospace Science and Technology, Politecnico di Milano, Via La Masa 34, 20156 Milano, Italy*

Abstract

A novel frequency–based optimization algorithm, suitable to tune generic controllers involved in the dual loop architectures, is presented. A control scheme, based on standard industrial regulators, is adopted to incorporate nonlinear constraints reproducing technological limitations, in a control surfaces actuation system installed on a wind tunnel aeroelastic demostrator. An integrated observer for disturbance rejection helps to meet one of the required constraints when aerodynamic loads are present. Numerical and experimental results are presented with the aim to design the actuation system and validate the methodology, considering both standard input signals and realistic command profiles.

Keywords: Aero–servo–elasticity, actuation system, industrial control, rate saturation, real–time

---

*Corresponding author

Email addresses: `alessandro.degaspari@polimi.it` (Alessandro De Gaspari), `andrea.mannarino@polimi.it` (Andrea Mannarino), `paolo.mantegazza@polimi.it` (Paolo Mantegazza)

[1]Post–doctoral Researcher

[2]Ph.D.

[3]Professor

Nomenclature

b	local airfoil semi-chord $[m]$
C	motor damping $[Nm \cdot s]$
$\mathsf{C}(s;\boldsymbol{p})$	transfer function of the controller
C_i	control transfer function of the inner loop
C_o	control transfer function of the outer loop
$C_{/p_k}$	control transfer function derivative w.r.t. the k-th optimization variable
$\mathbf{E}(j\omega)$	fictitious error array
$E_l(j\omega)$	fictitious error of the load loop
$E_m(j\omega)$	fictitious error of the motor loop
$E_{/p_k}$	fictitious error derivative w.r.t. the k-th optimization variable
$\mathbf{J}(j\omega)$	error Jacobian matrix
$\mathcal{J}$	optimization cost function
J_m	motor inertia $[Kg \cdot m^2]$
J_a	aileron inertia $[Kg \cdot m^2]$
K	motor stiffness $[N \cdot m]$
k	belt stiffness (tensioned side) $[N/m]$
$\mathsf{k_D}$	derivative gain of the aileron loop
$\mathsf{k_I}$	integral gain of the aileron loop
$\mathsf{k_P}$	proportional gain of the aileron loop
$\mathsf{k_I^m}$	integral gain of the motor loop
$\mathsf{k_P^m}$	proportional gain of the motor loop
$M(s)$	closed–loop transfer function
$M_l(j\omega)$	load closed–loop transfer function
$M_m(j\omega)$	motor closed–loop transfer function
N	filter cut–off frequency of the aileron loop $[Hz]$
$\mathsf{N_m}$	filter cut–off frequency of the motor loop $[Hz]$
$\boldsymbol{p}$	array of the control law parameters
$p_1, \ldots, p_8$	optimization variables
$r(s)$, $r(t)$	reference signal in the Laplace and time domain
r_1, r_2	pulley diameters $[m]$
$R_{l_{\boldsymbol{p}}}(j\omega)$	fictitious input of the load loop
$R_{m_{\boldsymbol{p}}}(j\omega)$	fictitious input of the motor loop
s	Laplace variable
$U(j\omega)$, $u(t)$	motor input signal in the Laplace and time domain
V_∞	asymptotic aerodynamic speed $[m/s]$
$Y_l(j\omega)$	output signal of the load loop
$Y_m(j\omega)$	output signal of the motor loop
α	belt pretensioning stiffness factor
θ_1	motor rotation $[rad]$
θ_2	aileron rotation $[rad]$
τ	gear ratio between motor and aileron pulley
ω	frequency of oscillation ($\omega = \Im(s)$) $[rad/s]$
ω_0	desired bandwidth
ω_r	reference motor rate

1. Introduction

During the design of control loops, actuators are usually considered linear, whereas their behavior is intrinsically nonlinear. In fact, even during normal operational conditions, they may saturate in position, e.g. the maximum reachable displacement or rotation, in rate, e.g. the maximum speed that an actuator is able to achieve, and in force, e.g. the maximum load that the actuation system is able to produce [1]. In addition, electro-hydraulic actuators may present other internal nonlinearities, such as free–play and friction [2], usually experienced during the motion of the actuation valves [3] and turbulent fluxes across valves and piston orifices [4]. Hysteresis is another phenomenon that can be found on this type of actuators [5]. Actuator failures can also result in significant deviation from the nominal dynamics and may cause departure in to highly nonlinear regimes [6]. These kind of saturations are intrinsically embedded by the physical limitations of the actuator components. When some sort of scaled testing is required, i.e. a wind tunnel experiment, actuators working on different physical principles are selected and these limitations are lost most of the time. However, when not accounted for, actuation system nonlinearities can reduce the performance of the control loop, eventually making it unstable.

In this work, actuator nonlinearities are reconstructed by an ad–hoc control law in the design of the control surfaces actuation system of a wind tunnel demonstrator. Such nonlinearities are introduced through the saturation of signals between two nested PID control loops. Because PID controllers are commonly used in practice, this methodology would allow a direct application to problems of industrial interest.

The control law tuning algorithm is one of the original contributions of this work. The proposed approach takes inspiration from the works [7, 8, 9, 10]. Such methods, labeled as data-driven, are based on the generation of a fictitious reference signal, which is generated recursively from a set of one-shot computational/experimental input-output data. The main difference with respect to model-based methods is that data-driven approaches do not attempt to identify the plant model, using instead the data produced by the plant to find the optimal controller setup. The cited methodologies can be divided in two groups:

- The Virtual Reference Feedback Tuning (VRFT) was first developed in [9] and then formalized in [11]. This approach selects a reference signal on the basis of a target system transfer function. This signal is then used to force the closed loop system to behave like the target through optimization iterations based on the data collected during the experiment.

- The Fictitious Reference Iterative Tuning (FRIT) is an automatic tuning method developed in [10]. Differently from the VRFT, where the reference signal is specified before starting the optimization, a virtual reference signal is computed recursively during the iterations, as the name might suggest.

The VRFT and the FRIT methods can be interpreted as different ways to formulate an optimization problem allowing to compute the controller parameters. In the case of the VRFT, it is the difference between the real input and the expected one to be minimized. Because of this, the VRFT is said to transform a control problem into an identification one. Regarding the FRIT instead, the optimization method minimizes the real output of the system and the one computed in closed loop during the optimization. Both methods are very flexible, in the sense that they could be employed for any controller structure, see for example [12] in the case of cascade controllers or [13, 14] for the tuning of neural controllers. Moreover, both method have been employed for tuning the so-called 2-degree-of-freedom controllers [15, 16].

An approach similar to the FRIT is pursued in this paper, including some substantial variations to the original method. Very similar optimization results were obtained using the VRFT method, but they are not presented here. The main difference of the present procedure with respect to the cited methods, which both work in the time domain, is the fact that the algorithm is written directly in the frequency domain thanks to the linearity of the control system when no saturation is activated. This change of domain allows a simpler formulation of the optimization problem, resulting beneficial also to the convergence speed of the method. A second contribution is the initialization of the control gains through the pole–placement procedure detailed in the following sections. According to the authors' knowledge, no similar method is available in the literature for a first–trial tuning of a nested PID controller based on a very few parameters of the physical system.

The test case considered in this work is the design of the control surfaces actuation system of a wind tunnel demonstrator within the EU funded project GLAMOUR (Gust Load Alleviation techniques assessment on wind tUnnel MOdel of advanced Regional aircraft). The aim of GLAMOUR, in response to the SP1-JTI-CS-2013-01-GRA-02-022 call, is the technological optimization and experimental validation through an innovative aeroservoelastic wind tunnel model of gust load alleviation control systems for the advanced

Green Regional Aircraft (GRA), developed by Finmeccanica Aircraft Division in the framework of Clean Sky Joint Technology Intiative.

The requirements that affect the design of the GLAMOUR servo–control systems descend directly from the Reference Aircraft (RA), that is the full–scale GRA, and include the related maximum bandwidth, rotation and rate saturation of each control surface. In order to introduce the desired rotation and rate saturation into the actuation system, a dual loop control architecture is adopted. The control system is tuned through the data–based optimization algorithm previously introduced. The robustness of the designed system is verified a posteriori using the classical gain and phase margin indicators. The control law is implemented through the real–time environment RTAI, also developed at the Department of Aerospace Science and Technology of Politecnico di Milano [17].

The general frequency–based optimization algoritm is detailed in section 2, while the specific dual loop architecture is described in section 3. The modeling of the aeroservoelastic/mechanical actuation system installed on the wind tunnel demonstrator is detailed in section 4, and the corresponding design is presented in section 5. Related results, including the experimental test bench activities, are reported in section 6.

2. Optimization Method

The procedure used to tune the parameters of the two controllers involved in the dual loop architecture takes inspiration from the works [7, 8, 9, 10]. Such methods are based on the generation of a fictitious reference signal, which is generated recursively given a set of one–shot computational/experimental input–output data. This is said to be a data–driven approach. In fact, it does not attempt to identify the plant model, instead it uses the data produced by the plant to find a controller, which generally is meant to minimize some control performance criterion. Nonetheless, despite the original idea of data–driven approaches, the closed loop transfer function can be experimentally identified through the collected data [10].

According to [11], if a controller $\mathsf{C}(s;\boldsymbol{p})$ results in a closed–loop system whose transfer function is $M(s)$, then, when the closed–loop system is fed by any reference signal $r(s)$, its output equals $M(s)r(s)$ in the frequency domain. Hence, a necessary condition for the closed–loop system to have the same transfer function as the target model is that the output of the two systems is the same for a given reference.
Standard modern reference design methods impose such a necessary condition by first selecting a reference $r(t)$ and then by choosing $\mathsf{C}(s;\boldsymbol{p})$ such that the condition is satisfied. However, for a general selection of $r(t)$, the above task is difficult to accomplish if a model of the plant is not available. The basic idea of the present approaches is to perform a wise selection of the reference signal so that the determination of the controller becomes easily achievable.
Considering the nomenclature of Fig. 1, the implemented optimization algorithm can be so resumed:

1. The collected input-output time domain data is transformed in the frequency domain through a FFT. Such signals will be referred as $U(j\omega)$, $Y_m(j\omega)$ and $Y_l(j\omega)$ respectively
2. Then, recursively:
   - Compute the fictitious input of the motor loop:
   $$R_{m_{\boldsymbol{p}}}(j\omega) = \frac{U(j\omega) + \mathsf{C}_\mathsf{i}(j\omega;\boldsymbol{p})Y_m(j\omega)}{\mathsf{C}_\mathsf{i}(j\omega;\boldsymbol{p})} \tag{1}$$
   - Compute the fictitious input of the load loop:
   $$R_{l_{\boldsymbol{p}}}(j\omega) = \frac{R_{m_{\boldsymbol{p}}}(j\omega) + \mathsf{C}_\mathsf{o}(j\omega;\boldsymbol{p})Y_l(j\omega)}{\mathsf{C}_\mathsf{o}(j\omega;\boldsymbol{p})} \tag{2}$$
   - Compute two fictitious errors $E_m(j\omega) = M_m(j\omega)R_{m_p}(j\omega) - Y_m(j\omega)$ for the motor and $E_l(j\omega) = M_l(j\omega)R_{l_p}(j\omega) - Y_l(j\omega)$ for the load

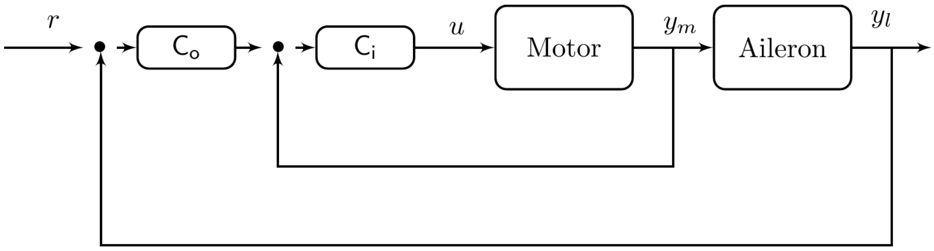

Figure 1: Generic dual loop controller

- Apply a nonlinear optimization algorithm to minimize the following cost function:

$$\mathcal{J} = \sum_{i=1}^{N} E_m^2(j\omega_i) + E_l^2(j\omega_i) \tag{3}$$

The details of the implemented optimization algorithm are described in the following lines. In this case, the optimization variables are the controllers gains, which are parameterized here as follows:

$$\mathsf{C_i} = p_1 + \frac{p_2}{j\omega}, \qquad \mathsf{C_o} = \frac{p_7 j\omega}{j\omega + p_8}\left(p_3 + \frac{p_4}{j\omega} + p_5 \frac{p_6 j\omega}{j\omega + p_6}\right) \tag{4}$$

The optimization algorithm used in this work is the Levenberg–Marquardt algorithm [18]. It basically requires the evaluation of the error and its gradient with respect to the optimization variables at each iteration of the optimization.

The error is clearly defined as:

$$\mathbf{E}(j\omega) = \begin{bmatrix} E_m(j\omega) \\ E_l(j\omega) \end{bmatrix} \tag{5}$$

While the computation of the gradient is more involved, with all the details provided here. Taking the derivative of $E_m(j\omega)$ and $E_l(j\omega)$ with respect to each optimization variable p_k, $k = 1, \dots, 8$, results in the following Jacobian matrix:

$$\mathbf{J}(j\omega) = \begin{bmatrix} E_{m/p_1}(j\omega) & E_{m/p_2}(j\omega) & \cdots & E_{m/p_8}(j\omega) \\ E_{l/p_1}(j\omega) & E_{l/p_2}(j\omega) & \cdots & E_{l/p_8}(j\omega) \end{bmatrix} \tag{6}$$

where $E_{/p_k}$ means the derivative of the error with respect to the k-th optimization parameter. Considering the definition of $E_m(j\omega)$ and $E_l(j\omega)$, their gradient with respect to the optimization variable p_k can be computed analytically:

$$\begin{aligned} E_{m/p_k} &= \frac{M_m}{\mathsf{C_i}^2}\left[\mathsf{C_i}\mathsf{C}_{\mathsf{i}/p_k} Y_m - \mathsf{C}_{\mathsf{i}/p_k}\left(U + \mathsf{C_i} Y_m\right)\right] \\ E_{l/p_k} &= \frac{M_l}{\mathsf{C_o}^2}\left[\left(\frac{\mathsf{C_i}\mathsf{C}_{\mathsf{i}/p_k} Y_m - \mathsf{C}_{\mathsf{i}/p_k}\left(U + \mathsf{C_i} Y_m\right)}{\mathsf{C_i}^2} + \mathsf{C}_{\mathsf{o}/p_k} Y_l\right)\mathsf{C_o} - \mathsf{C}_{\mathsf{o}/p_k}\left(R_{m_p} + \mathsf{C_o} Y_l\right)\right] \end{aligned} \tag{7}$$

where the dependence on the frequency is dropped to ease the reading.

At this point, the evaluation of the error gradient is performed through the computation of the terms $\mathsf{C}_{\mathsf{i}/p_k}$

and $\mathsf{C}_{\mathsf{o}/p_k}$, $k = 1, \ldots, 8$. This is detailed for C_{i}:

$$\begin{aligned} &\mathsf{C}_{\mathsf{i}/p_1} = 1 \\ &\mathsf{C}_{\mathsf{i}/p_2} = 1/j\omega \\ &\mathsf{C}_{\mathsf{i}/p_k} = 0 \qquad k = 3, \ldots, 8 \end{aligned} \tag{8}$$

and for C_{o}:

$$\begin{aligned} &\mathsf{C}_{\mathsf{o}/p_k} = 0 \qquad k = 1, 2 \\ &\mathsf{C}_{\mathsf{o}/p_3} = \frac{p_7 j\omega}{j\omega + p_8} \\ &\mathsf{C}_{\mathsf{o}/p_4} = \frac{p_7}{j\omega + p_8} \\ &\mathsf{C}_{\mathsf{o}/p_5} = -\frac{p_6 p_7 \omega^2}{-\omega^2 + (p_6 + p_8) j\omega + p_6 p_8} \\ &\mathsf{C}_{\mathsf{o}/p_6} = -\frac{p_5 p_7 j\omega}{j\omega p_8} \frac{\omega^2}{(j\omega + p_6)^2} \\ &\mathsf{C}_{\mathsf{o}/p_7} = \frac{j\omega}{j\omega + p_8} \left(p_3 + \frac{p_4}{j\omega} + p_5 \frac{p_6 j\omega}{j\omega + p_6} \right) \\ &\mathsf{C}_{\mathsf{o}/p_8} = -\frac{p_7 j\omega}{(j\omega + p_8)^2} \left(p_3 + \frac{p_4}{j\omega} + p_5 \frac{p_6 j\omega}{j\omega + p_6} \right) \end{aligned} \tag{9}$$

The error and its gradient can be defined at each frequency ω_i of interest, building the following elements used by the Levenberg-Marquardt algorithm:

$$\mathbf{E} = \begin{bmatrix} \mathbf{E}(j\omega_1) \\ \mathbf{E}(j\omega_2) \\ \vdots \\ \mathbf{E}(j\omega_N) \end{bmatrix} \qquad \mathbf{J} = \begin{bmatrix} \mathbf{J}(j\omega_1) \\ \mathbf{J}(j\omega_2) \\ \vdots \\ \mathbf{J}(j\omega_N) \end{bmatrix} \tag{10}$$

Collecting all the optimization variables in one vector $\mathbf{p}$, the j-th Levenberg–Marquardt iteration reads as:

$$\mathbf{p}_{j+1} = \mathbf{p}_j - \left(\mathbf{J}_j^{\mathrm{T}} \mathbf{J}_j + \lambda \mathbf{I} \right)^{-1} \mathbf{J}_j^{\mathrm{T}} \mathbf{E}_j \tag{11}$$

where $\mathbf{E}_j$ and $\mathbf{J}_j$ are the error and its gradient evaluated for $\mathbf{p}_j$. The coefficient λ is used to assure the non-singularity of the matrix $\mathbf{J}_j^{\mathrm{T}} \mathbf{J}_j$ and it is adjusted automatically during the iterations [18]. The algorithm is terminated when the norm of the relative variation between $\mathbf{p}_j$ and $\mathbf{p}_{j+1}$ is smaller than a given tolerance, in this case set to 10^{-4}.

It is clear that the bandwidth of C_{i} and C_{o} cannot be chosen arbitrarily, because they must guarantee that the inner loop has a significantly larger bandwidth than the outer one.
The two target models are chosen to be second order transfer functions of the type:

$$M(s) = \frac{\omega_0^2}{s^2 + 2\omega_0 + \omega_0^2} \tag{12}$$

In the following sections this tuning algorithm will be applied to the closed loop system of Fig. 3 and a comparison between the results obtained with a first estimate of the gains and those obtained with the refined controller will be provided.

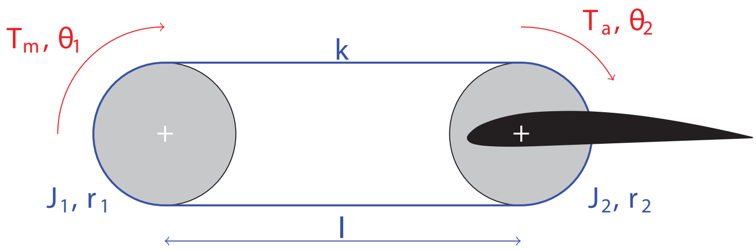

Figure 2: Belt drive system

3. The Dual Loop Architecture

The aircraft are usually equipped with actuation systems realized by means of electro–hydraulic actuators that show various saturating behaviors due to the physical limitations of their components. Because the wind tunnel model is constrained in size, small electrical motors are used to actuate its control surfaces. Such motors do not present any position saturation, while they may saturate in velocity but at values that are not in the range of interest. They also present a torque saturation that is related to the maximum current that can be applied to the motor. In order to adapt the related performance to one equivalent to the RA actuator, a specific control law, based on the dual loop approach, is defined in order to introduce the saturations experienced by the real system and to reproduce its dynamic behaviour.

Thanks to its wide application in industrial high precision tracking, a dual–loop strategy based on PID controllers is implemented [19]. The controller C_i of the motor (inner) loop described in Section 2 can be designed as a PI speed controller, making the actuator sufficiently fast to follow abrupt speed changes, e.g. possible rate saturations. The controller C_o of the load (outer) loop is a PID position controller, in order to assure the desired positioning precision within the required bandwidth. The rotation rate saturation is introduced in between the two control loops [20].

The electrical motors used in this work are coupled with a dedicated belt drive system because the lack of thickness inside the wing. From this point of view, the dual loop approach is the most suitable control architecture also to guarantee an accurate tracking, despite the combined action of the belt flexibility, indicated as k, and the aerodynamic load T_a acting on the aileron. A simplified model of the system used for the actuation of the ailerons is shown in Fig. 2.

The control architecture employs two position sensors, one on the motor side and one on the aileron side, as depicted in Fig. 3. The PID controller relates the control action $u(t)$ to the error between the current output and the reference signal through three parameters which are the proportional, derivative and integral gains. In this case the parameters of the aileron loop are $\mathsf{k_P}$, $\mathsf{k_D}$ and $\mathsf{k_I}$, respectively, while the parameters of the motor loop are $\mathsf{k_P^m}$ and $\mathsf{k_I^m}$. In order to guarantee that the discrete time realization of the controller does not deteriorate the effect of its derivative term, a filter with cut–off frequency $2\pi\mathsf{N}$ is included. The reference signal is the ω_r for the inner loop and $r(t)$ for the outer loop. The output signal is θ_2, properly filtered by a derivative term with cut–off frequency $2\pi\mathsf{N_m}$, for the inner loop and θ_1 for the outer loop.

Thanks to the feedback of θ_2, this architecture would allow an accurate tracking of the reference signal also in presence of unsteady disturbances, such as aerodynamic loads. As can be seen from Fig. 3, this dual–loop architecture allows the introduction of a rate saturation in between the two loops, so emulating the behavior of the actual electro–hydraulic actuator installed on the RA. This would have resulted impossible if only a single control on the motor side was implemented.

The tuning of the control system is carried out using the frequency–based optimization procedure detailed in Section 2, nevertheless, a first estimation of the control gains can be provided through an integrated analytical approach based on pole–placement theory [21]. The optimization will be carried out to further improve the performance of the closed loop system obtained by the pole–placement–based design.

Before beginning the analysis, a first comment is required. In the following steps, the motor rate is supposed to be measured. However, as clarified by Fig. 3, only the motor position is measured, and its speed is

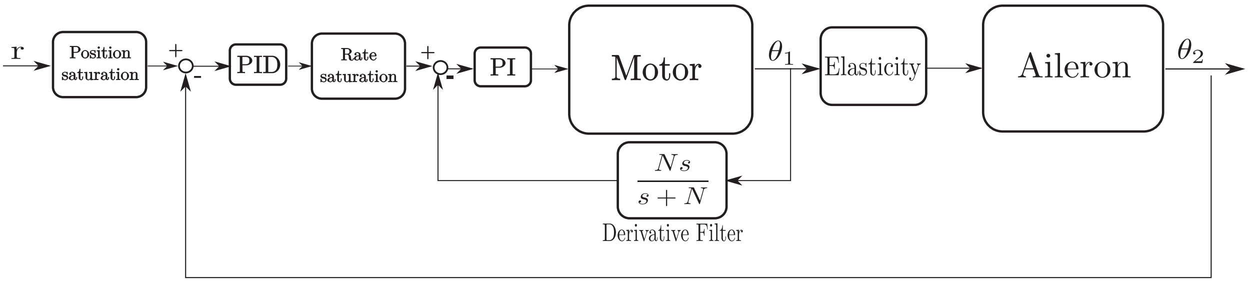

Figure 3: Dual loop controller.

estimated through the filter $\mathsf{N_m} s / (s + \mathsf{N_m})$ that has to be designed. Nevertheless, the rate speed will be supposed to be known, and the value of $\mathsf{N_m}$ will be set different from the value N, designed for its outer loop parent.

Now, consider the motor loop at first. This will be described by the following model in the frequency domain:

$$\left(Js^2 + Cs + K\right)\theta_1 = T_m = \left(\mathsf{k_P^m} + \frac{\mathsf{k_I^m}}{s}\right)\left(\omega_r - \frac{\mathsf{N_m} s}{s + \mathsf{N_m}}\theta_1\right) \tag{13}$$

where J is the total inertia, which considers both the motor inertia J_m and the one of the controlled surface J_a, according to the transport equation: $J = J_m + J_a/\tau^2$. The constant τ is the ratio between the different pulley diameters r_2 and r_1 represented in Fig. 2, required to transport the aileron rotation on the motor side. The constants C and K are the motor damping and stiffness, respectively. The various $\mathsf{k^m}$ and $\mathsf{N_m}$ are the motor gains and ω_r is the reference motor rate as can be observed from Fig. 3. Eq.(13) can be rewritten as:

$$\left[Js^2 + \left(C + \mathsf{k_P^m}\frac{\mathsf{N_m}}{s + \mathsf{N_m}}\right)s + \left(K + \mathsf{k_I^m}\frac{\mathsf{N_m}}{s + \mathsf{N_m}}\right)\right]\theta_1 = \left(\mathsf{k_P^m} + \frac{\mathsf{k_I^m}}{s}\right)\omega_r \tag{14}$$

The same equation can be rearranged as follows:

$$\left[Js^3 + (J\mathsf{N_m} + C)\,s^2 + (C\mathsf{N_m} + \mathsf{k_P^m}\mathsf{N_m} + K)\,s + \mathsf{N_m}\,(K + \mathsf{k_I^m})\right]\theta_1 = \frac{\mathsf{k_I^m}\mathsf{N_m}}{s} \cdot \frac{\left(\frac{\mathsf{k_I^m}}{\mathsf{k_P^m}} + s\right)}{\frac{\mathsf{k_I^m}}{\mathsf{k_P^m}}} \cdot \frac{(s + \mathsf{N_m})}{\mathsf{N_m}}\omega_r \tag{15}$$

To assign the system eigenvalues, a pole–placement approach based on prototyping the left hand side of Eq.(15) can be adopted. Considering the generic 3^{th} order low–pass filter:

$$s^3 + c_2\ \omega_{0,m}\ s^2 + c_1\ \omega_{0,m}^2\ s + c_0\ \omega_{0,m}^3 = 0 \tag{16}$$

where $\omega_{0,m}$ is the inner loop desired bandwidth. Imposing the equality of the two transfer functions coefficients, the following gains can be designed:

$$\begin{cases} \mathsf{N_m} & = \left(c_2\ \omega_{0,m}\ J - C\right)/J \\ \mathsf{k_I^m} & = \left(c_0\ \omega_{0,m}^3\ J - \mathsf{N_m}K\right)/\mathsf{N_m} \\ \mathsf{k_P^m} & = (c_1\ \omega_{0,m}^2\ J - \mathsf{N_m}C - K)/\mathsf{N_m} \end{cases} \tag{17}$$

At this point, the inner loop gains are designed and they are assumed to be constant. Considering the outer loop, it can be obtained connecting the full model, as it appears on the left hand side of Eq.(15), and the outer feedback contribution represented by the PID controller and the incoming signal $(r - \theta_2)$. According to the gear ratio assumption $\theta_1 = \tau\theta_2$, the outer system in closed loop is described by the following model in the frequency domain:

$$\left[Js^3 + (J\mathsf{N_m} + C)\,s^2 + (C\mathsf{N_m} + \mathsf{k_P^m}\mathsf{N_m} + K)\,s + \mathsf{N_m}\,(K + \mathsf{k_I^m})\right]\theta_2 = \left(\mathsf{k_P} + \frac{\mathsf{k_I}}{s} + \mathsf{k_D}\frac{\mathsf{N}s}{s+\mathsf{N}}\right)(r - \theta_2) \tag{18}$$

where the various k and N are the outer loop PID gains. The transformation from θ_1 to θ_2 is required because the signal tracking is performed through the aileron position, which differs from the motor one by the factor τ. The motor rate is transformed to the derivative of its position to allow the design of the outer position loop. Thanks to this assumption, the outer loop controller is so realized:

$$\omega_r = \tau\frac{s}{\mathsf{k_I^m}\mathsf{N_m}}\cdot\frac{\frac{\mathsf{k_I^m}}{\mathsf{k_P^m}}}{\left(\frac{\mathsf{k_I^m}}{\mathsf{k_P^m}} + s\right)}\cdot\frac{\mathsf{N_m}}{s+\mathsf{N_m}}\left(\mathsf{k_P} + \frac{\mathsf{k_I}}{s} + \mathsf{k_D}\frac{\mathsf{N}s}{s+\mathsf{N}}\right)(r-\theta_2) \tag{19}$$

In this way, a pole–zero cancellation is allowed to obtain the desired closed loop behavior.

The design of the outer PID loop and its gains can be completed by means of a 2^{nd} order approximation obtained dividing the left hand side of Eq.(18) by $\mathsf{N_m}$ and assuming $\mathsf{N_m}\to\infty$, while the full–order formulation will be used to perform simulations and verifications. The control law is designed such that:

$$\left[Js^2 + (C + \mathsf{k_P^m})\,s + (K + \mathsf{k_I^m})\right]\theta_2 = \left(\mathsf{k_P} + \frac{\mathsf{k_I}}{s} + \mathsf{k_D}\frac{\mathsf{N}s}{s+\mathsf{N}}\right)(r-\theta_2) \tag{20}$$

or equivalently:

$$\begin{aligned}&\left[Js^4 + (C + \mathsf{k_P^m} + J\mathsf{N})\,s^3 + (C\mathsf{N} + \mathsf{k_P^m}\mathsf{N} + K + \mathsf{k_I^m} + \mathsf{k_P} + \mathsf{k_D}\mathsf{N})\;s^2 +\right.\\ &\left.+\;(K\mathsf{N} + \mathsf{k_I^m}\mathsf{N} + \mathsf{k_P}\mathsf{N} + \mathsf{k_I})\,s + \mathsf{k_I}\mathsf{N}\right]\theta_2 = \left[(\mathsf{k_P} + \mathsf{k_D}\mathsf{N})\,s^2 + (\mathsf{k_P}\mathsf{N} + \mathsf{k_I})\,s + \mathsf{k_I}\mathsf{N}\right]r\end{aligned} \tag{21}$$

Once again, to assign the closed loop eigenvalues, a 4^{th} filter is considered:

$$s^4 + a_3\,\omega_0\;s^3 + a_2\,\omega_0^2\;s^2 + a_1\,\omega_0^3\;s + a_0\,\omega_0^4 = 0 \tag{22}$$

where ω_0 is the outer loop desired bandwidth. Imposing the equality between the coefficients of Eq.(22) and those of the left hand side of Eq.(21), the following gains can be computed:

$$\begin{cases}\mathsf{N} &= (a_3\,\omega_0\;J - C - \mathsf{k_P^m})\,/J\\ \mathsf{k_I} &= a_0\,\omega_0^4\;J/\mathsf{N}\\ \mathsf{k_P} &= \left(a_1\,\omega_0^3\;J - \mathsf{N}K - \mathsf{N}\mathsf{k_I^m} - \mathsf{k_I}\right)/\mathsf{N}\\ \mathsf{k_D} &= \left(a_2\,\omega_0^2\;J - \mathsf{N}C - K - \mathsf{N}\mathsf{k_P^m} - \mathsf{k_I^m} - \mathsf{k_P}\right)/\mathsf{N}\end{cases} \tag{23}$$

Once the gains are so computed, the outer loop is designed and the Eq.(19) can be used to perform the tracking of reference rotations. The outer PID is multiplied by three different parts working as one derivative and two filters, resulting in a very efficient system which offers two main advantages: it does not require any anti–windup scheme and allows to reduce the noise providing a very clean command signal to the inner loop.

This method gives a first estimation of the controller gains that can be refined through the frequency–based optimization detailed in Section 2. Nevertheless, numerical experiments proven that such an estimate is already a good starting point for the closed loop design.

4. Aeroservomechanical modelling

The mathematical model related to the system of Fig. 2 can be written following basic physical principles:

$$\begin{cases} J_m\ddot{\theta}_1 + C\dot{\theta}_1 + \alpha k r_1^2\theta_1 - \alpha k r_1 r_2 \theta_2 = T_m \\ J_a\ddot{\theta}_2 - \alpha k r_1 r_2\theta_1 + \alpha k r_2^2\theta_2 = T_a \\ \ddot{x}_a + a_{a,1}\dfrac{V_\infty}{b}\dot{x}_a + a_{a,2}\dfrac{V_\infty^2}{b^2}x_a = b_{a,0}\theta_2 + b_{a,1}\dot{\theta}_2 + b_{a,2}\ddot{\theta}_2 \\ T_a = c_a x_a + d_{a,0}\theta_2 + d_{a,1}\dot{\theta}_2 + d_{a,2}\ddot{\theta}_2 \end{cases} \tag{24}$$

The constant α is introduced to take into account the fact that, in the rubber belt of Fig. 2, its compressed side might not work at all as the other one is under tension ($\alpha = 1$) or it could present some kind of residual stiffness ($1 < \alpha \leq 2$) thanks to the presence of an internal reinforcement. As can be noticed from the last two equations of Eq.(24), an unsteady aerodynamic model is used to compute the hinge moment acting on the control surface. The model is developed starting from the work of Theodorsen [22], transforming the frequency–based model presented in such a work into a state–space one. Therefore, the constants c_a, $d_{a,i}$, $a_{a,i}$ and $b_{a,i}$ can be directly computed following [22], while all the other variables are obtained from the mechanical system design.
This aeromechanical system is connected to the servocontrol scheme depicted in Fig. 3 in order to have the corresponding mathematical model of the complete system.
However the particular control architecture considered is not able to follow precisely the requested rate saturation introduced to reproduce the effects of the technological limitations, but it stabilizes at a lower value as soon it reaches such a limitation. This is due to the presence of the aerodynamic disturbance. In fact the outer PID loop is able to reject efficiently constant or slowly varying disturbances only, thanks to its integral term. The problem is, while the controller tries to maintain the rotation rate constant during the saturation, the aerodynamic hinge moment changes because it depends also on the control surface rotation, as well represented by Eq.(24). Because of this, the controller is not able to perform the task related to the tracking of the command signal during the rate saturation. Nevertheless, the chosen framework is essential for integrating possible rate saturations as required by the project specifications.
A possible solution to this problem would be the introduction of an additional control term able to compensate time–varying disturbances. In this work a solution based on the use of a reduced order observer is devised, as in [23]. Starting from the measure of the motor position $\theta_{1,\text{meas}}$ the observer integrates the following dynamic model:

$$\begin{cases} J\ddot{\theta}_1 = T_m + d \\ \dot{d} = w \end{cases} \tag{25}$$

where d is the disturbance perturbing the motor actuation, while w is a white noise signal. Therefore d includes the effect of the aerodynamic disturbance and other possible effects, e.g. dry friction, that may deteriorate the controller action. An estimation of such a disturbance and its following integration into the control law would result into a beneficial effect, especially near saturating conditions. The observer has the following structure:

$$\begin{Bmatrix} \dot{\theta}_1 \\ \ddot{\theta}_1 \\ \dot{d} \end{Bmatrix} = \begin{bmatrix} 0 & 1 & 0 \\ 0 & 0 & J^{-1} \\ 0 & 0 & 0 \end{bmatrix} \begin{Bmatrix} \theta_1 \\ \dot{\theta}_1 \\ d \end{Bmatrix} + \begin{bmatrix} 0 \\ J^{-1} \\ 0 \end{bmatrix} T_m + \begin{bmatrix} 0 \\ 0 \\ 1 \end{bmatrix} w + \begin{bmatrix} L_1 \\ L_2 \\ L_3 \end{bmatrix} (\theta_{1,\text{meas}} - \theta_1) \tag{26}$$

where L_i, are the elements of the observer gain matrix. This system is tuned through a classical LQG design [24], where the weight matrices used in this case are $\mathbf{Q} = \text{diag}\left(0, 0, 7 \cdot 10^5\right)$ and $R = 1 \cdot 10^{-6}$. As can be noticed from Eq.(26), the observer not only provides an estimate of the disturbance but also a direct calculation of the motor rate $\dot{\theta}_1$, which has proven to be more accurate and robust than the estimation computed by the linear filter of Fig. 3. In view of these results, the final architecture of the controller is depicted in Fig. 4.

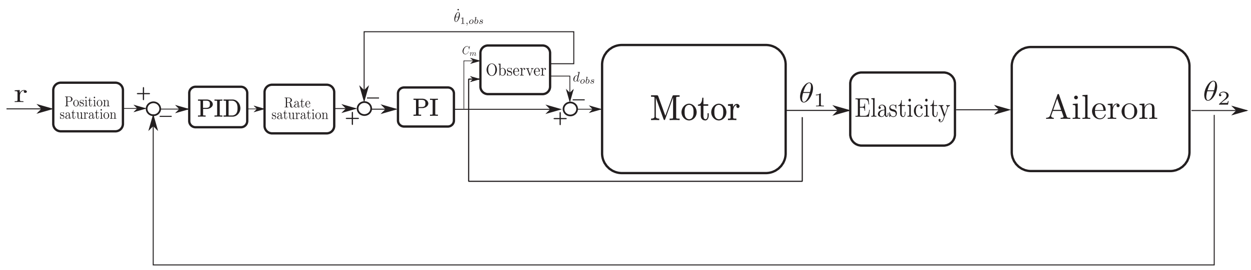

Figure 4: Dual loop controller with integrated observer for disturbance rejection

5. Application to the Wind Tunnel Demonstrator

The methodology proposes in the previous sections is applied to the design of the actuation system installed on the GLAMOUR wind tunnel demostrator. Because of the lack of room inside the scaled wing and the non–conventional control surfaces configuration, the actuation systems is composed by two motors that drive two independent ailerons by the reinforced rubber belts, while the elevator is directly actuated by one motor placed outside the wind tunnel model and rigidly connected to the stabilizer. The wing and the horizontal tail, where the two ailerons and the elevator actuators are installed on, are shown in Fig.(5). Driven by previous experiences in the design of actuation systems for wind tunnel models [25], particular focus is given to the design of the actuation system of one aileron, with the others that can be considered very similar. Only the design of the inboard aileron control is presented in this work, being the most challenging one. The elevator does not require the use of any drive belt, which may introduce compliance in the system, while the outer aileron is subjected to lower aerodynamic forces. Despite the elevator shaft is directly connected to the corresponding motor shaft, the dual loop architecture is the same one, described in Section 3. Indeed, it is necessary to introduce the required rate saturation in between the two loops.
The experimental setup included the design and the assembly of the same hardware system which will be installed on the wind tunnel demonstrator, the use of the same real–time environment. The experimental apparatus, composed by the hardware and the electronics used to command the actuation system of the three control surfaces, is shown in Fig. 6. It includes one PC, three actuators, two for the ailerons and one for the elevator, connected to as many drives and four power supplies. Each drive needs two power lines, one for the electronics and the other one for the motor power. The additional power supplies are connected to the digital PCI board and to the digital channels of the drive. The PC is equipped with four PCI boards: the digital board, the analog input board, that allows to receive the command input from the gust alleviation control system, the analog output board and the encoder board.
The motor position (inner loop) is measured through the encoder already embedded in the motor itself, while the aileron position (outer loop) is measured by a precision conductive plastic potentiometer, as shown in Fig. 7. This last signal is conditioned through an anti–aliasing filter, whose cut–off frequency is set at 200 Hz. The control law is implemented through the real–time environment RTAI [17].

5.1. Mechanical Design

The definition of the design requirements in terms of bandwidth and maximum torque acting on the motors is based on the results obtained from two different simulations: the aeroelastic analysis performed on the Finite Element Model (FEM) of the complete wind tunnel demonstrator, including all three control surfaces; the simulations performed on the mathematical model described in section 4 on each control surface actuation system, including the closed–loop servo–control. Considering an appropriate safe margin, following design values, in terms of required torque, were adopted for the aileron and the elevator actuators: 0.9 Nm and 6 Nm. Two different motors were selected, respectively. For the aileron, the *Harmonic Drive*® *RSF–5B*

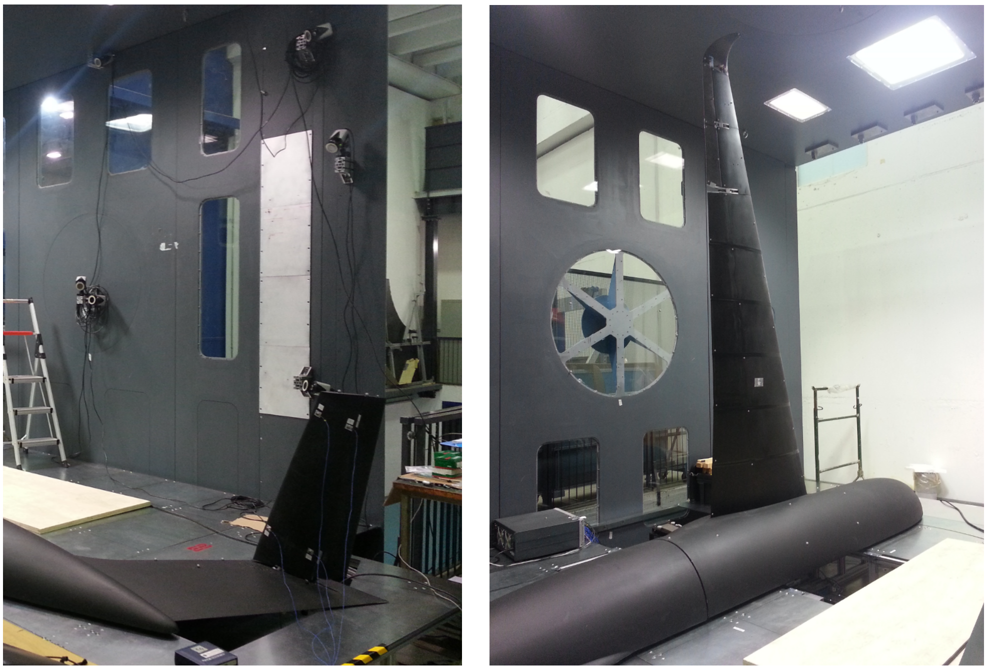

Figure 5: Complete wind tunnel model (left) and aeroelastic wing (right) where the actuation system is installed.

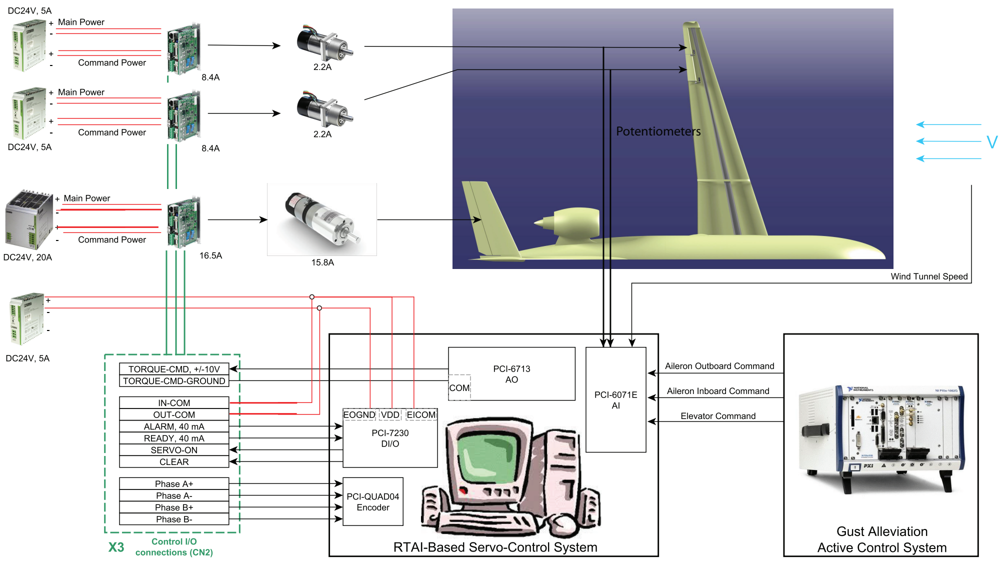

Figure 6: Experimental apparatus scheme and hardware of the GLAMOUR wind tunnel model.

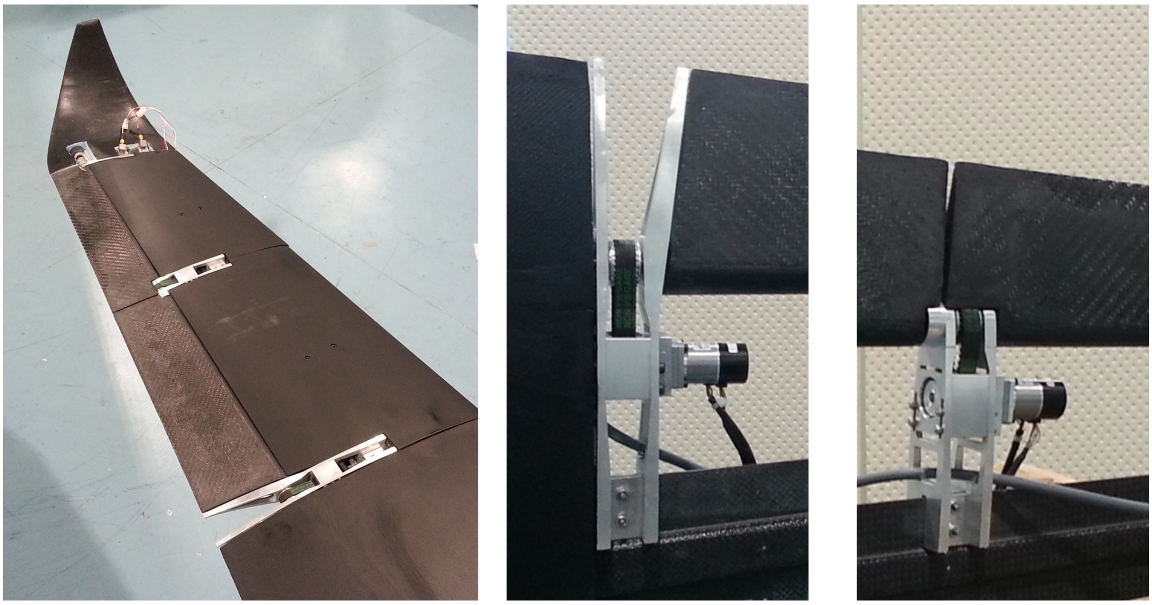

Figure 7: Aileron actuation system installed on the wing.

J_m [kg m ^{2}]	J_a [kg m ^{2}]	C [Nm/rad/s]	r_1 [m]	r_2 [m]	k [N/m]	b [m]
$1.8308 \cdot 10^{-4}$	$2.5048 \cdot 10^{-4}$	0.03	$7.285 \cdot 10^{-3}$	$1.1105 \cdot 10^{-2}$	$5.8378 \cdot 10^{5}$	0.15

Table 1: Belt drive main data

with a gear ratio of 50 and an additional gear ratio due to the pulleys contribution allows to produce the required torque. In the case of the elevator, the *Harmonic Drive®* *RSF–11B* with a gear ratio of 50 is directly able to generate the required torque. Harmonic Drive® was selected due to the high performance attributes of its gearing technology which includes zero backlash, high torque, compact size, and excellent positional accuracy. Standard metric *HTD–3M* timing belts were chosen for this application. Considering the wind tunnel design conditions and corresponding safety margins, the gear ratio $\tau = 22/14$, due to the different number of teeth on the large and small pulley respectively, allows to produce a maximum torque of 1.41 Nm on the large pulley which is directly connected to the ailerons. Considering the wing taper ratio, two different belt lengths were selected for the inboard and outboard aileron belt drive: the center distance between the small and large pulleys is 47.85 mm and 37.3 mm respectively. In order to not exceed the permissible total span tension, 9 mm wide belts were chosen.

The mechanical/structural design of the actuation system was led following an integrated approach that involved the design of the wing and the horizontal tail of the wind tunnel demonstrator. The outer part of the wing is also used for the experimental verification of the complete actuation system. Fig. 7 shows the wing region where the aileron actuation system is installed, together with the *Harmonic Drive®* motors and the ribs which are used to house all the mechanical system in a compact solution able to perfectly fit the external wing shape.

The mechanical quantities corresponding to the inboard aileron system are defined in Table 1 and they are used for the design and simulations of the control system presented in this work. The architecture of the other actuation systems is the same, as well as the optimization procedure which was applied to all three systems, providing three different set of controller parameters.

Several analyses have been carried out to study the influence of the parameter α, while the results presented here are all related to $\alpha = 1$ to show that the control system is able to perform its functions properly also in

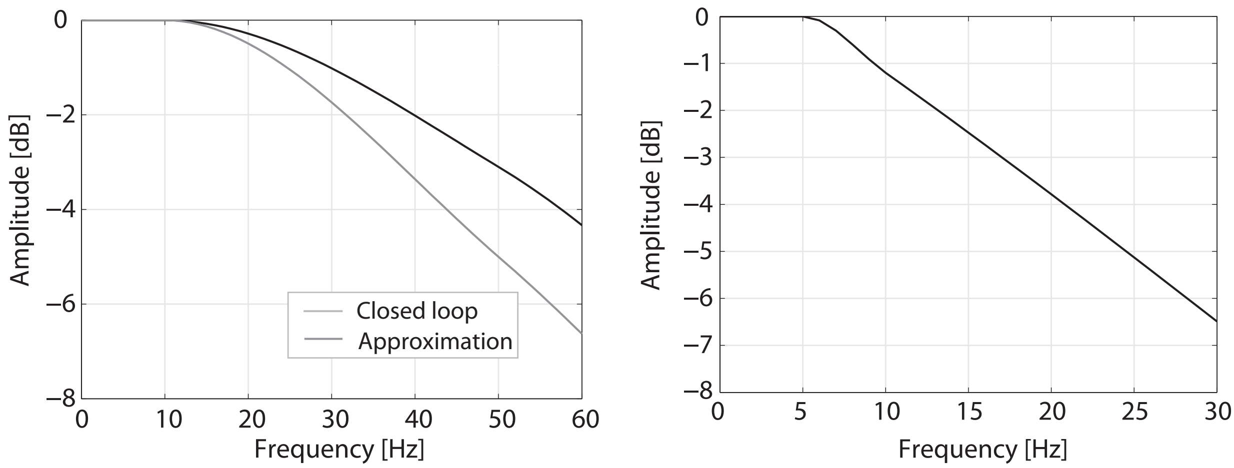

(a) Inner loop design

(b) Outer loop design

Figure 8: Pole–placement–based design

such a pessimistic situation. Using these values, the mechanical system of Fig. 2 shows a natural frequency of 106 Hz related to the belt flexibility, which is outside the bandwidth of interest.

5.2. Control Tuning

The mathematical model 24 is used for the design of the controller. The tuning procedure of Section 2 is applied to the control system of Fig. 3. Starting from the initial guess estimated through the pole–placement procedure detailed in Section 3, the previously described optimization algorithm is applied to refine all the controller parameters, i.e. k_P^m, k_I^m, N_m, k_P, k_I, k_D and N. The controller is then applied through its discrete implementation, performed at a control frequency of 1250 Hz. Furthermore, because the response of the aeroelastic system described by Eq.(24) depends on the wind tunnel speed, a rough gain scheduling of the controller has been required. Three speeds have been considered: 0, 27.44 and 34.3 m/s which are the wind tunnel speed used for the test of the gust alleviation system, correctly scaled from the design flight conditions of the RA. The tuning simulations shown here are relative to the highest speed.

The closed loop system is first tuned by means of the pole–placement–based design method, described in Section 3, to have an inner bandwidth of 50 Hz and an outer bandwidth of 20 Hz. The inner loop control gains are determined by prototyping the denominator, i.e., the closed–loop poles, of the left hand side of Eq.(15), according to a 3^{th} order Bessel filter. The inner loop desired bandwidth $\omega_{0,m} = 50\ Hz$ is used in Eq.(16) and divided by the coefficient $C_{in} = 1.7557$ for converting Bessel parameters, that have been normalized to unit delay at $\omega = 0$, to 3 dB attenuation at 1 rad/s [26]. The outer loop control gains are determined by prototyping the left hand side of Eq.(21). The 4^{th} order filter of Eq.(22) was obtained by the product of two 2^{nd} order Bessel filters, with a bandwidth of 20 Hz and 50 Hz, respectively. Both values are divided by the coefficient $C_{out} = 1.3617$ for converting Bessel parameters, as described in [26]. The results of the pole–placement–based design in terms of final closed loop response are shown in Fig. 8, where the inner loop design is reported together with its 2^{nd} order approximation used for the outer loop design, as represented by Eq.(20). Corresponding phase margin is 42 deg at 11 Hz. This preliminary estimation represents a good starting point because the motor inertia is known with a high degree of accuracy. The high inner bandwidth permits the controller to follow abrupt speed changes. The outer bandwidth allows to match the dynamic requirements coming from the RA.

Starting from the collected input–output data, the frequency–based optimization was applied to the complete system in order to refine the controller gains considering a sort of Hardware–in–the–loop (HIL) technique. While the mechanical parts of the system, including the electrical motors, are the physical ones installed on the wing, the aerodynamic loads acting on the control surfaces are emulated by the

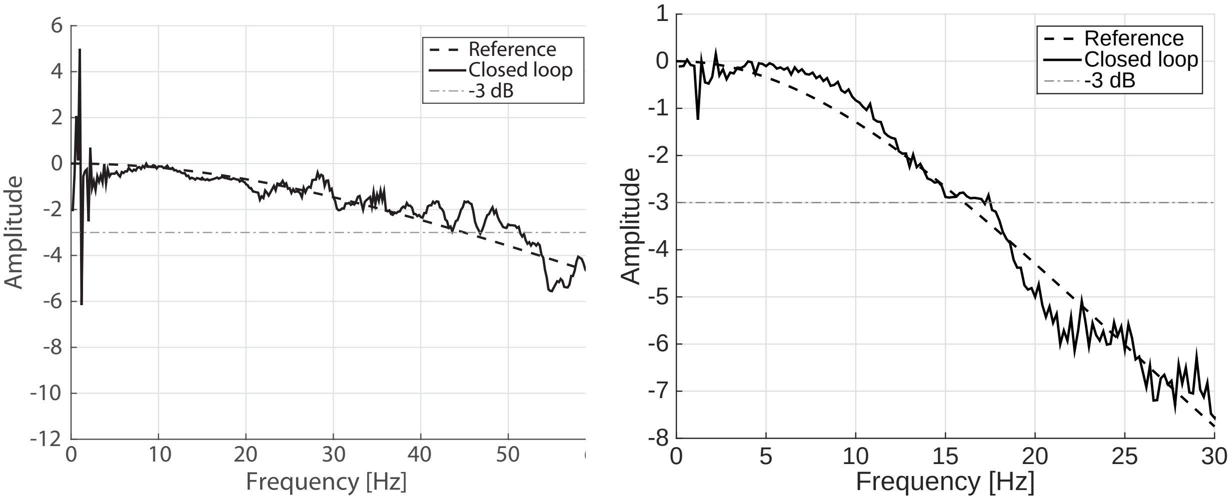

(a) Inner loop experimental optimization

(b) Outer loop experimental optimization

Figure 9: Optimization of the control loops by experimental data

	k_P^m	k_I^m	N_m	k_P	k_I	k_D	N
Pole–placement	0.17	24	89	0.728	346.639	0.0046	60
Experimental optimization	0.055	6.2	300	0.701	534.14	0.0041	205

Table 2: Controller gains

aerodynamic model of Eq.(24), getting the required data related to aileron rotation (θ_2, $\dot{\theta}_2$ and $\ddot{\theta}_2$) directly from the potentiometer measures. After several test simulations, a sweep excitation of 1 deg up to 150 Hz, is employed as training signal by the HIL platform and used by the optimization algorithm presented in Section 2, always setting the target inner loop bandwidth at 50 Hz and the outer loop bandwidth at 20 Hz. These values are related to the structural mode frequencies of the wind tunnel demonstrator, but they are mainly due to the bandwidth requirements which descend from the performances of the actuator installed on the RA. The resulting optimized closed loop transfer functions are depicted in Fig. 9, while the obtained gains value are listed in Table 2 and compared with their initial guess coming from the pole–placement–based design. Even if the data is noisy, the optimization is able to bring the closed loop response close enough to the target. The optimization algorithm mainly modifies the inner loop gains and the value of the filters constants, i.e. N_m and $\frac{k_I^m}{k_P^m}$, taking them to the maximum value allowed by the optimization. This is probably due to the aerodynamic effects, not included in the pole–placement–based model. The outer loop gains are sligtly modified, in particular the values of k_P appears very close. This could be due to a high stiffness of the actual belt, which is considered as rigid in the pole–placement–based design. Therefore a similar proportional gain is required to maintain the same performance on the experimental apparatus. The obtained closed loop gain margin together with the phase margin, which is 38 deg at 11 Hz, guarantees a good level of robustness, in the face of possible system uncertainties, and allows to match the dynamic behavior of the electro–hydraulic actuator installed on the RA.

6. Results

After the control gains are optimized, position and rate saturations are introduced in the model to represent also the technological limitations of the RA actuation system. In particular the torque/rate saturation diagram, characterizing the electro–hydraulic actuators, was incorporated into the model as nonlinear limitations. In order to check the capability of the controller when such nonlinearities are excited, different signals were considered and different tests were performed. In the following subsections, corresponding numerical and experimental verifications are reported.

6.1. Simulations

At the first, the closed loop system is tested considering the tracking of a simple sine of amplitude 10 deg and frequency 3 Hz. Such a case presents large rate and continuous saturations and therefore is a good benchmark for the present control system to reproduce the wanted rate saturation without introducing any kind of instability. The results are reported in Fig. 10, where a comparison between the controller designed through the pole–placement technique and the optimized one is considered. In this paper, all the results are normalized with respect to their related saturation values. As can be seen, the rate saturation does not allow an adequate tracking of the command signal, and both designs lead to very similar outputs. However, the designed inner loop is sufficiently fast to permit an efficient rate saturation, as shown in Fig. 10(c). Always considering the same figure, it is clear that the optimized controller is able to suppress the oscillations around the saturation value much more efficiently than the pole–placement design method. This is due to the fact that optimized controller is tuned on the real input–output data of the system, while the pole–placement design considers a very approximate model of the system dynamics that does not even take into account the presence of the elastic belt.

Once proven that the control system is able to simulate the presence of rate saturations, the tracking properties are tested on a more realistic signal. In order to test the capability of the controller also with aerodynamic loads, we consider one of the signals coming from the gust suppression law, designed in [27, 28]. Because the aerodynamic loads act as a disturbance in the present control design, and because they depend on the wind speed, the controller gains are scheduled at the three wind tunnel test speeds, using the same procedure detailed previously. The particular control architecture considered in this work is characterized by a small overshoot which appears in the step response at the high wind tunnel speed. This phenomenon is found to be typical for this scheme and other solutions, i.e. a classical dual loop controller [19], would not produce such an overshoot. Nevertheless, the chosen framework is essential for integrating possible rate saturations as required by the project specifications.

A test performed at $V_\infty = 34.3\, m/s$ is shown in Fig. 11, where the aileron rotation and rate are normalized with respect to their imposed saturation limits. As can be seen from Fig. 11(a), both controllers present good tracking properties, while the optimized one improves the performance in terms of a faster tracking responses near the saturations. Moreover, as shown in Fig. 11(b), it is able to follow the saturation in rate with a sufficiently good accuracy. When the rate saturation is active, the designed system introduces the corresponding delay in the aileron positioning that is recovered as soon as the rotation rate goes back under the saturation level. Indeed, the integration of the observer described in Section 4, allows to reject the time–varying disturbances due to the aerodynamic loads.

6.2. Experimental Tests

The same Hardware–in–the–loop (HIL) technique described in section 5.2 was adopted to finally test the functionality and the capabilities of the actuation system before starting the wind tunnel compaign, even simulating the presence of the aerodynamic forces. At first, a sine signal of frequency 2 Hz and sufficiently small amplitude to avoid rate saturation is used as reference. This test is used to verify if the apparatus presents reasonable performance and does not exhibits unusual behaviors. The second test considers as reference a sine signal of frequency 4 Hz that will induce rate saturation in the servo. This test is used to verify if the experimental apparatus presents a good rate saturation performance. The results are displayed in Fig. 12, where the experimental output signal is compared to the tracked reference and the outcome of the simulator due to the same input signal.

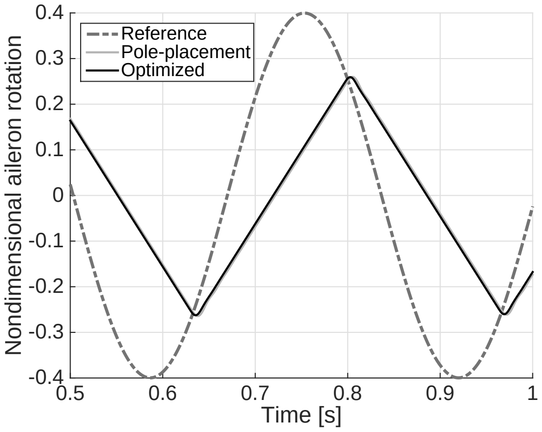

(a) Command tracking

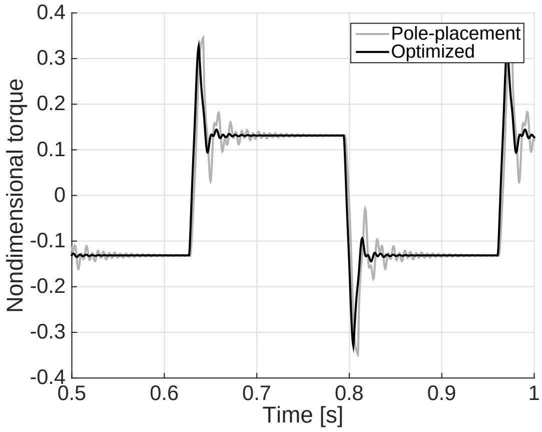

(b) Control input

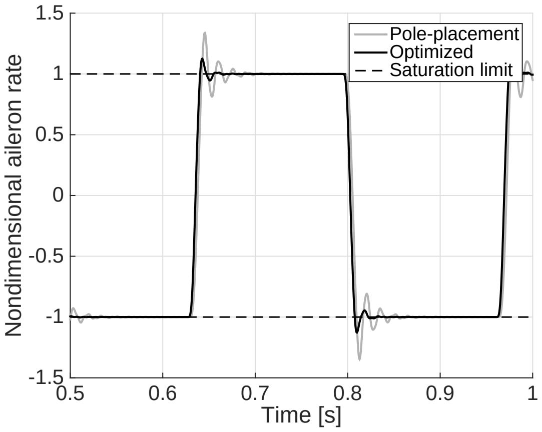

(c) Aileron rotation rate

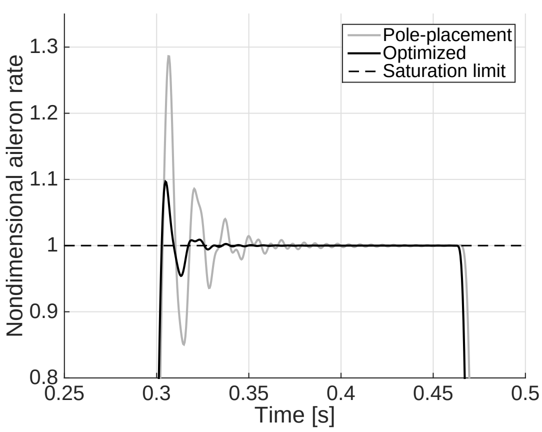

(d) Close-up near the saturation

Figure 10: Tracking of a sine of amplitude 10 degrees and frequency 3 Hz

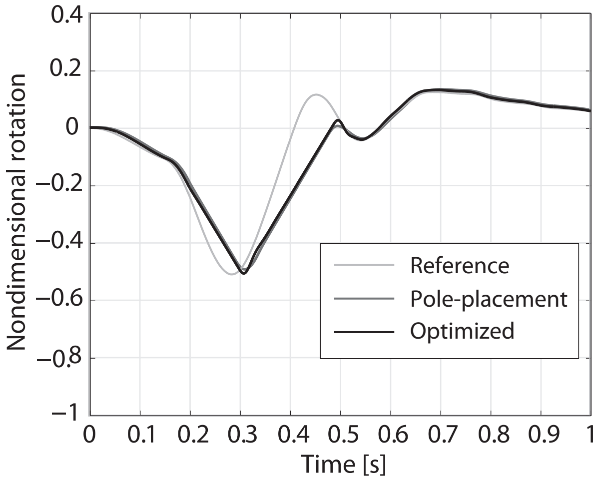

(a) Command tracking

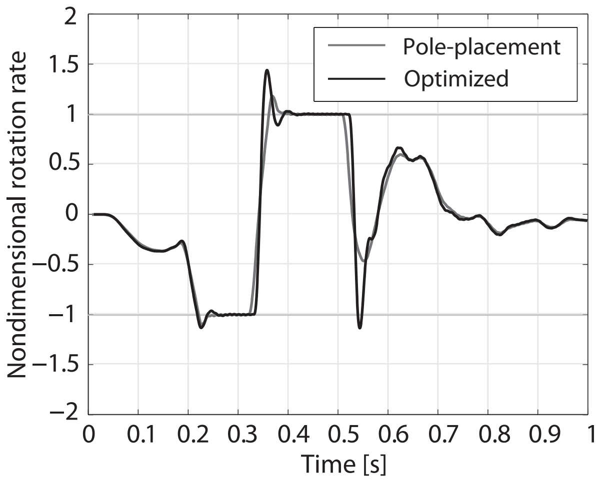

(b) Aileron rotation rate

Figure 11: Tracking of a gust suppression signal at $V_\infty = 34.3\,m/s$ with torque compensation

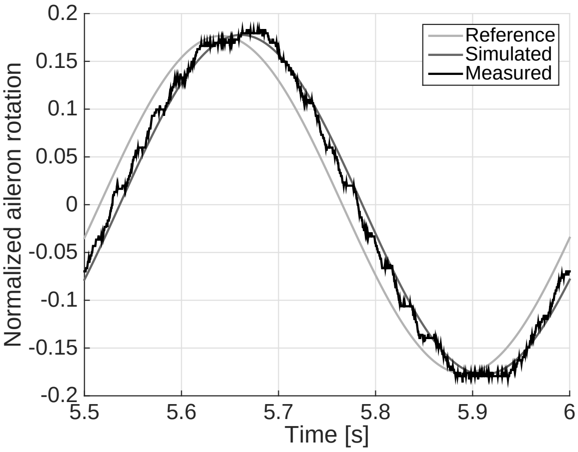

(a) 2 Hz aileron rotation

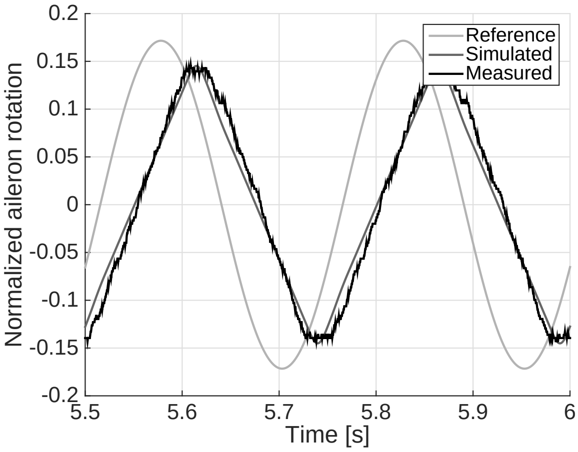

(b) 4 Hz aileron rotation

Figure 12: Experimental tracking of sine signal

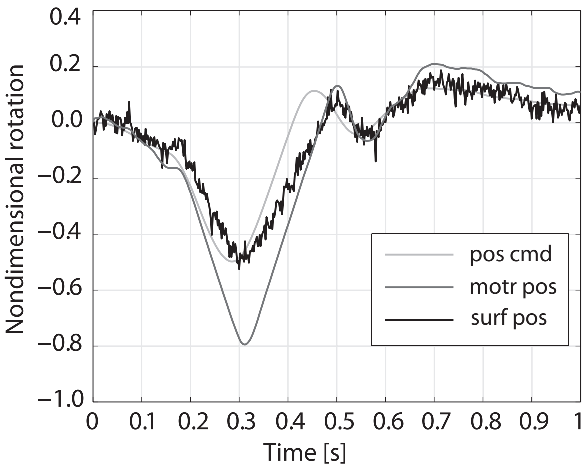

(a) Motor and aileron rotation

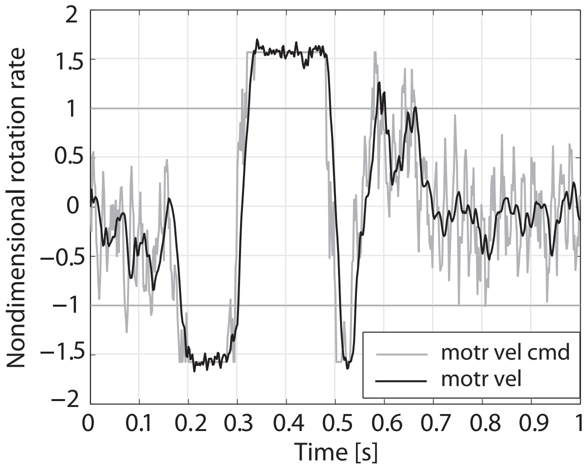

(b) Motor rotation rate

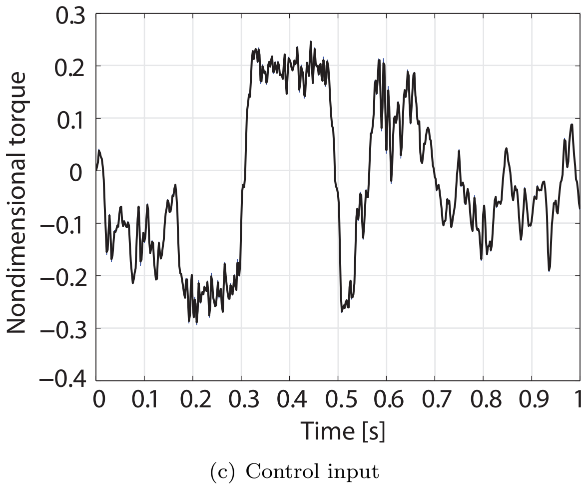

(c) Control input

Figure 13: Experimental tracking of the gust suppression signal

The servo system presents good tracking properties, with a response very similar to that predicted by the simulator. The simulator is able to capture the main dynamic behavior of the implemented servo. Nevertheless, even if an anti–aliasing filter is present, oscillations, not so evident in the simulations, apppear in the potentiometer signal. This can be due to a quite high level of dry friction which characterizes the Harmonic Drive® motors, i.e. about 8% of the saturation torque. On the one hand these actuators ensure zero backlash and an excellent positional accuracy, on the other hand they require a control effort slightly larger than the one predicted by the simulator.

The last test considers the gust suppression input previously used in the simulator design. The outcomes are shown in Fig. 13, where the tracked reference, the main motor signals and the corresponding aileron signals are compared. The tracking of the aileron rotation and the motor rotation rate is very accurate, as shown in Fig.(13). Here, the position command r is labeled as pos cmd, the motor position Y_m as motr pos and the aileron position Y_l as surf pos. The motor rate command, coming out from the PID controller, is labeled as motr vel cmd, while the motor rate coming from the derivative filter placed in the inner feedback, is labeled motr vel.

As anticipated in section 3, on the one hand the inner controller is sufficiently fast to follow abrupt speed changes, as the rate saturation depicted in Fig.(13(b)). On the other hand, the outer controller is able to assure the desired positioning, as depicted in Fig.(13(a)). As soon as the rate saturation is finished, the aileron position follows the reference signal again. Moreover the tracking after the rate saturation is better than the simulated one, shown in Fig.(11(a)). Some jitters are present in both responses, but they do not depend on the aerodynamic, since they appear also in the tracking shown in Fig.(12), where the wind is turned off. When the nonlinear actuation is belt driven, such jitters may be common. In the case of this work, the nonlinearities and the belt drive are combined with the dry friction of the selected motors. The oscillations in the signals are noticible when the rotation rate is very small, approximately zero, and the dry friction effects can be dominant, inducing to an unforeseen control effort.

7. Conclusions

In the present effort, the control surfaces actuation system of a wind tunnel aeroelastic aircraft model has been modeled numerically, aiming at designing a control law with guaranteed bandwidth and robustness. Simple controllers such as PIDs have been chosen, with the nonlinear constraints imposed by the actuators of the real Reference Aircraft making the design more involved. As a matter of fact, the intrinsic compliance of the actuation system and the requested rate saturations have forced the controller architecture to be composed by a dual–loop PID, with the motor side commanded in speed while the aileron is commanded in position. A novel frequency–based optimization has been proposed to tune both controller loop using a single experiment. Numerical simulations have been used to support these claims, showing that an integrated observer for disturbance rejection is also required to satisfy robustly the constraint on the rate saturation. The complete actuation system was validated through an experimental test campaign and the related results coming have been presented.

The results shows that the design of the servo system leads to a robust experimental implementation, avoiding unstable behaviors and respecting the design constraints of the actuation system.

The present actuation system is finally integrated in the wind tunnel aeroelastic demonstrator which will be used to validate different control strategies aimed at alleviating aeroelastic vibrations due to incoming gusts.

8. Acknowledgement

The research leading to these results has received funding from the European Community's Seventh Framework Programme (FP7/2007-2013) for the Clean Sky Joint Technology Initiative under Grant Agreement for Partners no. 620084

References

[1] M. Matsutani, A. Annaswamy, L. G. Crespo, Adaptive Control in the Presence of Rate Saturation with Application to a Transport Aircraft Model, in: AIAA Guidance, Navigation and Control Conference, 2010.

[2] A. Mannarino, An Adaptive Compensation Strategy of Control Surfaces Free–Play, in: AIAA Guidance, Navigation, and Control Conference, 2015, pp. 1 – 20. doi:10.2514/6.2015-0612.

[3] M. Farenzena, J. O. Trierweiler, Valve backlash and stiction detection in integrating processes, in: 8th IFAC International Symposium on Advanced Control of Chemical Processes, 2012.

[4] H. Merritt, Hydraulic Control Systems, Wiley, 1967.

[5] X. Xu, Y. Gao, W. Zhang, Aeroelastic dynamic response and control of an aeroelastic system with hysteresis nonlinearities, Journal of Control Science and Engineering (2015).

[6] K. Sibilski, J. Zurek, W. Wroblewski, Influence of free-play and friction in control system on aircraft flight dynamics, in: 26th International Congress of the Aeronautical Sciences, 2008.

[7] M. Safonov, T.-C. Tsao, The unfalsified control concept and learning, IEEE Transactions on Automatic Control 42 (1997) 843–847.

[8] J. Myungsoo, M. Safonov, Automatic PID tuning: an application of unfalsified control, in: Proceedings of the IEEE International Symposium on Computer Aided Control System Design, 1999, pp. 328–333. doi:10.1109/CACSD.1999.808669.

[9] G. Guardabassi, S. Savaresi, Virtual reference direct design method: an off-line approach to data-based control system design, IEEE Transactions on Automatic Control 45 (2000) 954–959.

[10] S. Masuda, M. Kano, Y. Yasuda, A fictitious reference iterative tuning method with simultaneous delay parameter tuning of the reference model, Proceedings of the IEEE International Conference on Networking, Sensing and Control (2009) 422 – 427.

[11] M. Campi, L. Lecchini, S. Savaresi, Virtual reference feedback tuning: a direct method for the design of feedback controllers, Automatica 38 (2002) 1337 – 1346.

[12] F. Previdi, D. Belloli, A. Cologni, S. Savaresi, Virtual Reference Feedback Tuning (VRFT) Design of Cascade Control Systems with Application to an Electro-Hydrostatic Actuator, in: 5th IFAC Symposium on Mechatronic Systems, 2010.

[13] Y. Li, J. Shen, Direct Nonlinear Controller Design Based on Virtual Reference and Support Vector Machine, in: Power and Energy Engineering Conference, 2009, pp. 1–4.

[14] A. Esparza, A. Sala, Application of neural networks to virtual reference feedback tuning controller design, in: 3rd IFAC Workshop on Advanced Fuzzy and Neural Control, 2007.

[15] O. Kaneko, Y. Wadagak, S. Yoshitake, S. Yamamoto, FRIT for Non-Miminimum Phase Systems in the 2-DOF Control Architecture: Simultaneous Attainment of Controllers and Models, SICE Journal of Control, Measurement, and System Integration 7 (2014) 35–40.

[16] O. Kaneko, Y. Yamashina, S. Yamamoto, Fictitious reference tuning for the optimal parameter of a feedforward controller in the two-degree-of-freedom control system, in: IEEE International Conference on Control Applications, 2010.

[17] R. T. A. Interface, https://www.rtai.org/?Homepage, Technical Report, Department of Aerospace Science and Technology, Politecnico di Milano, 2015.

[18] D. Marquardt, An algorithm for least-squares estimation of nonlinear parameters, Journal of the Society for Industrial and Applied Mathematics 11 (1963) 431–441.

[19] J. Tal, Two feedback loops are better than one, Machine Design. http://machinedesign.com/archive/two-feedback-loops-are-better-one (1999).

[20] A. De Gaspari, A. Mannarino, P. Mantegazza, Design and realization of the control surfaces actuation system within the glamour project, in: AIDAA2015, XXIII Conference of the Italian Association of Aeronautics and Astronautics, Torino, Italy, 2015, pp. 1 – 15.

[21] M. Andrighettoni, P. Mantegazza, Multi-input/multi-output adaptive active flutter suppression for a wing model, Journal of Aircraft 35 (1998) 462–469.

[22] T. Theodorsen, I. E. Garrick, Nonstationary flow about a wing-aileron-tab combination including aerodynamic balance, Technical Report, NACA Technical Report No. 736, 1942.

[23] C. D. Johnson, Accomodation of external disturbances in linear regulator and servomechanism problems, IEEE Transactions on Automatic Control 16 (1971) 635–644.

[24] B. Friedland, Control System Design: An Introduction To State-Space Methods, Dover Publications, 2005.

[25] A. De Gaspari, S. Ricci, L. Riccobene, A. Scotti, Active aeroelastic control over a multisurface wing: Modeling and wind-tunnel testing, AIAA Journal 47 (2009) 1995–2010.

[26] C. Bond, Bessel Filters: Polynomials, Poles and Circuit Elements, Technical Report, 2003.

[27] F. Fonte, S. Ricci, P. Mantegazza, Gust load alleviation for a regional aircraft through a static output feedback, Journal of Aircraft (2015) 1–16.

[28] R. Veiberman, M. Weiss, M. Karpel, F. Fonte, L. Travaglini, S. Ricci, Aeroservoelastic response of nonlinear wind tunnel model to non–uniform gust field, in: AIAA SciTech, 57th AIAA/ASCE/AHS/ASC Structures, Structural Dynamics, and Materials Conference, San Diego, California, USA, 2016, pp. 1 – 14. doi:10.2514/6.2016-1486.